Scattering of Quasistatic Plasmons From One-Dimensional Junctions of Graphene: Transfer Matrices, Fresnel Relations, and Nonlocality

Vyacheslav Semenenko,[1] Mengkun Liu,[2] and Vasili Perebeinos[1,*]

[1] *Department of Electrical Engineering, University at Buffalo, The State University of New York, Buffalo, New York 14260, USA*

[2] *Department of Physics and Astronomy, Stony Brook University, Stony Brook, New York 11794, USA*

(Received 10 February 2020; revised 25 June 2020; accepted 24 July 2020; published 18 August 2020)

We consider eigenmodes of one-dimensional quasistatic plasmons in periodic graphene structures with junctions of three different types. From the numerical solutions of Maxwell's equations, we reconstruct the transmission and reflection coefficients for single junctions, which are in perfect agreement with the available analytical results. Using our method, we calculate reflections from the double-junction structures and compare them with the semiphenomenological transfer-matrix approach based on the corresponding single-junction solutions. Limitations of the latter approach in designing plasmon resonators and waveguides based on graphene or other two-dimensional conducting materials are discussed.

DOI: 10.1103/PhysRevApplied.14.024049

I. INTRODUCTION

Graphene is an ideal material for conducting and processing electrical signals due to its high carrier mobility, surface-plasmon wave confinement, and excellent electrical tunability [1–10]. As in the case of microwave and optical communication engineering, reflection of collective plasmon excitations among different circuit elements is essential.

Plasmon scattering in graphene one-dimensional (1D) junctions was studied recently both theoretically [11–17] and experimentally [18–20]. In particular, the following types of junctions have been discussed: (1) an abrupt interface, i.e., the discontinuous doping level of the two-dimensionl (2D) material [12,13] [see Fig. 1(a)]; (2) local inhomogeneity, namely, scattering off a discontinuity gap [11,21] [see Fig. 1(b)], and on a corrugation [22]; (3) discontinuity of the dielectric constant in underlying substrate [15,16] [see Fig. 1(c)]. Those studies of the individual junctions allow extensions to the more complex structures with multiple junctions within the scattering and transfer-matrix approach.

However, because of the nonlocality of the equations describing the charge carrier density dynamics in 2D conducting materials [23], the scattering waves with amplitudes B_1 and A_2 [as shown in Fig. 2(a)] are not influenced by the evanescent waves, provided that the distances of interest are greater than some characteristic length scale L_{e12} and L_{e21} away from the junction. Our studies verify an intuitive hypothesis that the characteristic lengths depend only on the plasmon properties at the corresponding sides of the junction:

$$L_{e12} = \frac{\lambda_{p1}}{2}, \quad L_{e21} = \frac{\lambda_{p2}}{2}, \tag{1}$$

where $\lambda_{p1,2}$ are the corresponding plasmon wavelengths outside of the junction.

Similarly, in the case of transmission through a double-junction barrier, one can assume that a transfer matrix (T matrix) constructed from the solution of the individual barriers scattering problem is applicable, provided that the separation L between the barriers is larger than the plasmon wavelength λ_{p0} [as shown in Fig. 2(b)]. However, we find that the minimum length L, when the T matrix model is still applicable, is not always limited by λ_{p0}, but it also depends on the plasmon wavelengths outside of the junction region, i.e., $\lambda_{p,\pm 1}$.

II. COMPUTATIONAL DETAILS

In this work, we develop a method for retrieving scattering coefficients of graphene plasmon junctions. The method is based on the assumption that the T-matrix approach is applicable in structures with multiple junctions. We do the calculations for the variable length L between the two junctions. Initially, we choose L to be much bigger than any of the three plasmon wavelengths, i.e., in the region between the junctions, and on both sides of this region [as shown in Fig. 2(b)]. Then we gradually reduce L to find the conditions when the T-matrix approach ceases to be valid. Neglecting retardation effects (i.e., considering quasistatic plasmons) and transforming

*vasilipe@buffalo.edu

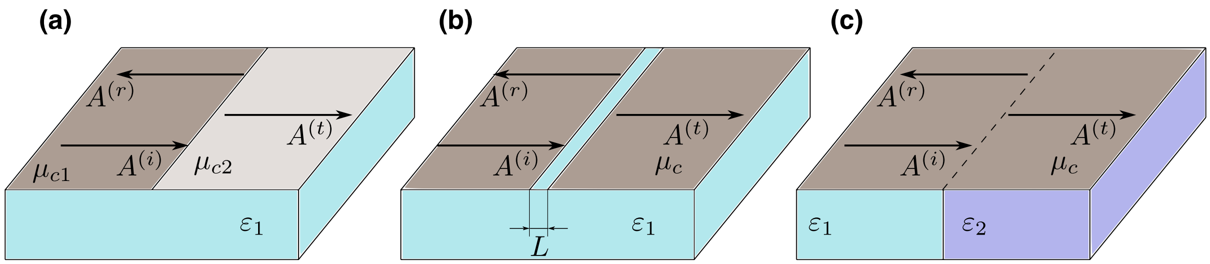

FIG. 1. Schematic view of the three junction geometries: (a) discontinuity in the doping level, (b) gap in graphene, and (c) discontinuity in the underlying substrate.

geometries in Fig. 1 to the periodic arrays (as shown in Fig. 3) enables us to study multiple junctions and to employ the Fourier expansion for the plasmonic modes' solution. As a result, the problem is reduced to a standard eigenvalue-eigenvector problem. The quasistatic approximation preserves the nonlocality of the equations, and it is valid due to the small radiative losses during the scattering event [24]. Typical plasmon wavelengths in graphene are in the range of 150–200 nm, which are 2 orders of magnitude smaller than the corresponding light wavelengths at the plasmon's frequencies.

The propagating plasmon mode is determined by the charge-carrier density distribution in graphene that, in general, can be written as $\sigma_{\omega,q}(x,t) = \mathrm{Re}\left\{\sigma_0 e^{i\omega t - iqx}\right\}$, where σ_0 is the complex amplitude, ω is the frequency, and q is a wavevector. A relationship between ω and q is given by a solution of the following dispersion equation [25]:

$$\frac{\omega}{i\gamma_\omega} = \frac{2\pi q}{\varkappa}, \quad \varkappa = \frac{\varepsilon_a + \varepsilon_b}{2}, \tag{2}$$

where ε_a and ε_b are dielectric permittivities of the media above and below graphene, correspondingly. The conductivity of graphene γ_ω is taken here according to the Drude model [26]:

$$\gamma_\omega = \frac{e^2 \mu_c}{\pi \hbar^2 (i\omega + \nu)}, \tag{3}$$

where μ_c is the Fermi energy in graphene, and ν is the electron scattering rate. In the area, that is at least a few plasmon wavelengths $\lambda_p = 2\pi/q$ away from the junction, the total charge-carrier density can be represented by a linear combination of running waves $\sigma_{\omega,q}$ and $\sigma_{\omega,-q}$ in opposite directions. Therefore, the amplitudes $A^{(i,r,t)}$ in Figs. 1(a)–1(c) describe the complex charge-carrier density waves, spreading in the designated directions labeled by (i,r,t): incident, reflected, and transmitted, correspondingly. We define the reflection and transmission coefficients ρ and τ as the ratios $\rho = A^{(r)}/A^{(i)}$ and $\tau = A^{(t)}/A^{(i)}$.

In a more general case, when waves impinging upon a junction from both sides [see Fig. 2(a)], the incoming and the outgoing waves are related with each other by the scattering matrix:

$$\begin{bmatrix} A_2 \\ B_1 \end{bmatrix} = S_{12} \begin{bmatrix} A_1 \\ B_2 \end{bmatrix}, \quad S_{12} = \begin{pmatrix} \tau_{12} & \rho_{21} \\ \rho_{12} & \tau_{21} \end{pmatrix}. \tag{4}$$

It can be shown directly from the analytical expressions [12], that at least in the case of a discontinuous-conductivity junction the ρ and τ coefficients do not have a similar structure as Fresnel's coefficients in optics. For example, the well-known relations $\rho_{12} = -\rho_{21}$ and $\tau_{12}\tau_{21} - \rho_{12}^2 = 1$ are no longer satisfied. Nonetheless, analogously to the quantum-mechanics scattering, the scattering matrices are governed by the following relation (see Ref. [27]):

$$S_{12} \cdot S_{21}^* = I, \tag{5}$$

where I is the identity matrix, the dot means matrix multiplication, and the asterisk means elementwise complex conjugation. It reflects a generalized form of Fresnel's relations known from optics. In the case of real coefficients ρ and τ, Eq. (5) reduces to Fresnel's relations. In the case of scattering of a local inhomogeneity [see Fig. 1(b)], when $\rho_{12} = \rho_{21} = \rho$ and $\tau_{12} = \tau_{21} = \tau$, Eq. (5) gives a trivial relation $|\rho|^2 + |\tau|^2 = 1$ expressing the energy flux conservation as well as a less obvious relation $\tau\rho^* + \rho\tau^* = 0$, which means that if $\rho \neq 0$ and $\tau \neq 0$, it is mandatory for both of them to have nonzero imaginary parts.

We employ the Fourier expansion method [23,25] to solve self-consistently Maxwell's equations for the electrostatic field and the charge-carrier density in graphene in a periodic array of junctions shown in Figs. 3(a)–3(c).

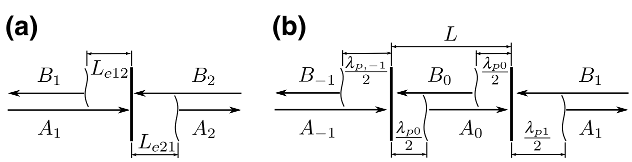

FIG. 2. Sketch of the individual (a) and double (b) junctions with propagating waves with amplitudes A_k, B_k scattered by them. The wiggling lines show the characteristic distances at which evanescent waves fade away.

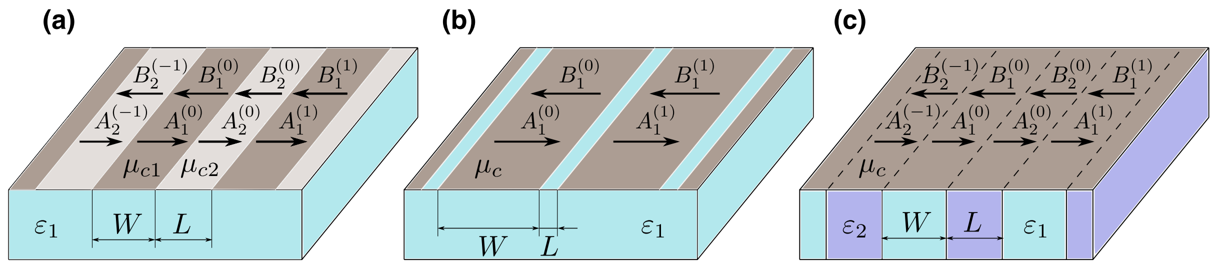

FIG. 3. The geometries adapted for numerical calculations and studying interference between closely located junctions corresponding to the junction types depicted in Fig. 2.

According to Bloch's theorem, any unknown solution $\sigma(x,t)$ can be represented as

$$\sigma(x,t) = \mathrm{Re}\, e^{i\omega t - iKx}\sigma_{\omega 0}(x), \tag{6}$$

where K is a quasimomentum and $\sigma_{\omega 0}$ is a periodic function with the period $d = W + L$, see Appendix A.

In Fig. 4, we show one of the eigenmodes, which depends only on the size parameters W, L, and the phase shift $\Phi = Kd$ between the oscillations in the adjacent unit cells due to the quasistatic approximation considered here. The phase shift is introduced to avoid singularity in the equations for the complex reflection and transmission coefficients. The plasmon wave amplitudes A_k and B_k, shown in Figs. 3(a)–3(c), can be found by fitting a numerical solution to a combination of the running waves spreading in both directions (see Appendix A):

$$\sigma_{\omega 0}^{(\mathrm{model})}(x) = A\exp\left[-iq(x - x_L)\right] + B\exp\left[iq(x - x_R)\right], \quad x \in [x_L + L_{\mathrm{ind}} .. x_R - L_{\mathrm{ind}}], \tag{7}$$

where A and B are the amplitudes of the propagating waves moving to the right and to the left, correspondingly in a given region between the two junctions; x_L and x_R are x coordinates of the junction boundaries; q is the plasmon wavevector; and L_{ind} is the indentation from a junction needed to bound the region at which the fitting with the combination of propagating waves is possible. Here, we use $L_{\mathrm{ind}} = \lambda_p/2$ (half wavelength of a plasmon in the region between the junctions) and make sure that the residual of fitting:

$$\mathcal{E}_{\mathrm{fit}} = \sqrt{\frac{1}{N_p}\sum_{k=1}^{N_p}\left|\sigma_{\omega 0}(x_k) - \sigma_{\omega 0}^{(\mathrm{model})}(x_k)\right|^2} \tag{8}$$

is always low enough; here N_p is the number of data points for which the curve fitting is done. Numerically obtained eigenmodes $\sigma_{\omega 0}(x)$ are normalized by $\max|\sigma_{\omega 0}(x)|$ before fitting. Plasmonic modes at the geometries in Figs. 3(a) and 3(c) have two regions where the fits and their errors $\mathcal{E}_{\mathrm{fit}1,2}$ are calculated.

Using the superposition principle, one can construct S matrices S_{12} [or S_{11} for the case of the geometry shown in Fig. 3(b)] from the known plasmon wave amplitudes, see details in Appendix B. To make sure that the result is correct, we analyze two more residuals based on the energy-flux conservation $\mathcal{E}_{\mathrm{P}}$ (see details in Appendix B) and error in the scattering matrix $\mathcal{E}_{\mathrm{SM}}$:

$$\mathcal{E}_P = |1 - R - T|, \quad \mathcal{E}_{\mathrm{SM}} = \sum_{i,j=1,2}\left|\left\{S_{12}\cdot S_{21}^{*} - I\right\}_{ij}\right|, \tag{9}$$

where R and T are the energy-flux reflection and transmission coefficients.

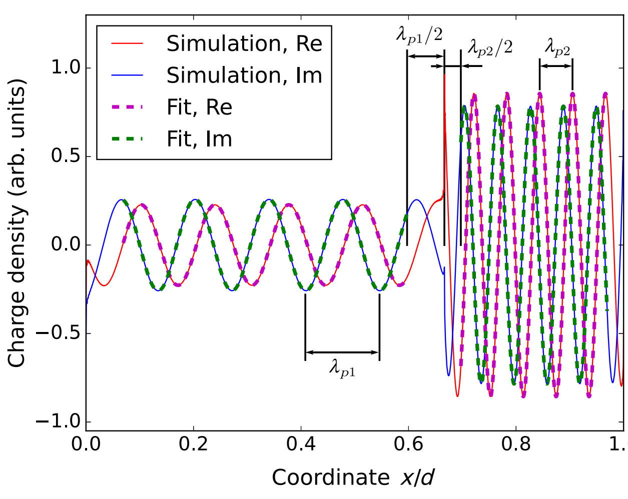

FIG. 4. Example of the numerical solution along with the fits to Eq. (B3) in the case of a discontinuous-substrate geometry [see Fig. 1(f)] for the following parameters: $W = 1000$ nm, $L = 500$ nm, $\varepsilon_1 = 3.9$, $\varepsilon_2 = 10$, and $\Phi = 0.6\pi$. $L_{\mathrm{ind}1}$ and $L_{\mathrm{ind}2}$ are the indentation lengths determining the ranges at which the curve fitting is done. λ_{p1} and λ_{p2} are plasmon wavelengths in two regions of the unit cell. The fit error defined by Eq. (8) is equal to $\log_{10}\mathcal{E}_{\mathrm{fit}} = -2.75$. The number of Fourier harmonics is $N = 1500$.

III. RESULTS FOR SCATTERING BY SINGLE JUNCTIONS

The results of our numerical method for the scattering coefficients in the three cases of junctions shown in Fig. (1) are presented in Fig. 5. In the quasistatic approximation, the refection in the cases of discontinuous doping and substrate does not depend on frequency. We use a mode with the smallest $\mathcal{E}_P$ for a given set of arguments (μ_{c2}/μ_{c1} or ε_2). The average decimal logarithms of residuals $\mathcal{E}_{\text{fit}}$, $\mathcal{E}_P$, $\mathcal{E}_{\text{SM}}$, and their standard deviations are calculated over all the data points presented in the corresponding panels. Very small values of the fit error (approximately 10^{-3}) in all three cases prove our assumption of the criteria in Eq. (1).

We find numerically, as seen from the plots in Fig. 5(a) and 5(c), that for the asymmetric junctions, the relation $|\rho_{12}| = |\rho_{21}|$ always takes place, which is a consequence of Eq. (5).

For the cases of discontinuous-doping and gap-in-graphene junctions, analytical solutions are available [12, 21]. The former in our notation reads

$$\rho_{12} = e^{-i\vartheta}\frac{1-\alpha}{1+\alpha}, \quad \tau_{12} = \frac{2\sqrt{\alpha}}{1+\alpha}\sqrt{\frac{s_1}{s_2}}, \quad \vartheta = \frac{\pi}{4} - \frac{2}{\pi}\int_0^{\infty}\frac{\arctan(\alpha u)\, du}{1+u^2}, \quad \alpha = \frac{\mu_{c2}}{\mu_{c1}}, \tag{10}$$

where $s_k \propto \mu_{ck}^2$ (see the details in Appendix B). The latter is given by

$$\rho = \frac{i\pi}{i\pi - C - \log(\pi L/2\lambda_p)}, \quad L \ll \lambda_p, \tag{11}$$

where $C = 0.855\cdots$ is Euler's constant. They are shown by the solid curves in Figs. 5(a) and 5(b) and they agree perfectly with the results obtained using our numerical method.

In the case of a discontinuous substrates, a simple analytical expression is not available. Using results from Ref. [16] applicable in the $|\rho_{12}| \ll 1$ limit and results from Ref. [12], we develop a phenomenological model:

$$|\rho_{12}| = \frac{\left|\lambda_1^{\alpha} - \lambda_2^{\alpha}\right|^{\beta}}{\left(\lambda_1^{\alpha} + \lambda_2^{\alpha}\right)^{\beta}}, \quad \lambda_{i=1,2} = (\varepsilon_0 + \varepsilon_i)^{-1}, \tag{12}$$

which works extremely well when $\varepsilon_2 \gtrsim \varepsilon_1$, as shown in Fig. 5(c). The only two adjustable parameters α and β are given in Table I. The clear dependencies of α and β on the substrate's dielectric permittivity confirm the point presented in Ref. [16] that the function $\rho_{12}(\varepsilon_1, \varepsilon_2)$ does not have a simple analytical scaling even in the quasistatic case, which neglects scattering into radiative modes.

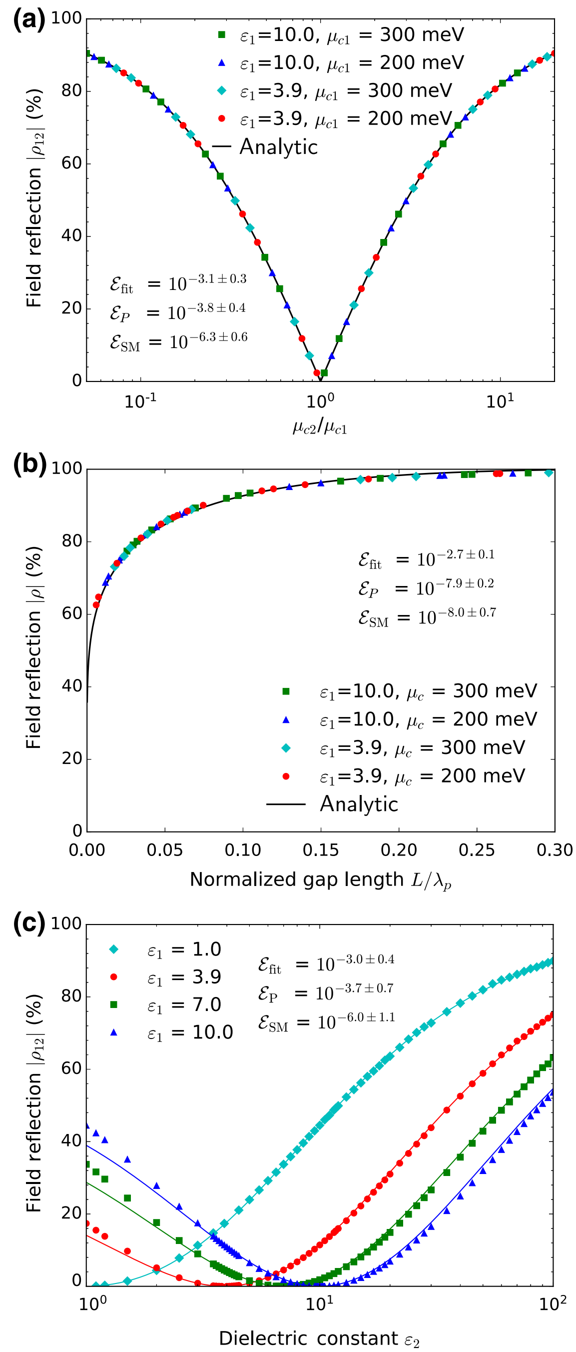

FIG. 5. Numerically (markers) and analytically (solid lines) calculated field reflection coefficient's $|\rho_{12}|$ scaling relations in the cases of (a) discontinuous-doping-level junction versus the ratio of the Fermi energies; (b) gap-in-graphene junction versus the ratio of the gap's width to plasmon wavelength in graphene. (c) Numerically calculated (markers) and fit of the model function in Eq. (12) (solid lines) in the case of discontinuous-substrate junction versus dielectric permittivity ε_2. Four fixed values of the dielectric permittivity ε_1 of the substrate under incident and reflected plasmon areas are used. Fit parameters (α, β) are given in Table I. Fermi energy of graphene in the calculations is given as $\mu_c = 300$ meV, but the result does not depend on this value. In all our calculations, dielectric permittivity of the medium above graphene is $\varepsilon_0 = 1$.

TABLE I. Fit parameters in Eq. (12) giving the absolute values of the reflection coefficients in the case of a discontinuous-substrate junction shown in Fig. 1(c).

ε_1	α	β
1	0.896	1.829
3.9	0.856	1.948
7	0.834	1.914
10	0.847	1.959

IV. SCATTERING BEYOND THE ISOLATED JUNCTION LIMIT

The conditions, when the numerical methods used for calculating dependencies in Fig. 5 converge, are directly related to the question of the interaction of neighboring junctions. While the numerical accuracy depends on parameters such as Fourier harmonics truncation number N and the indentation lengths for the fits L_{e12} and L_{e21} shown in Fig. 2(a), the resulting scattering coefficients are strongly dependent also on the number of plasmon wavelengths fit in the plasmon-supporting regions n_1, n_2 and the number of the longer wavelengths fit in the shorter region ψ:

$$n_1 = \frac{W}{\lambda_{p1}}, \quad n_2 = \frac{L}{\lambda_{p2}}, \quad \psi = \frac{\min\{W, L\}}{\max\{\lambda_{p1}, \lambda_{p2}\}}. \tag{13}$$

The presented results in Fig. 5 are calculated for $n_1, n_2, \psi \gtrsim 10$. The comprehensive analysis of the numerical results in three-dimensional parameter space $n_1, n_2, \psi \lesssim 10$ burdens the narrative of this work. Therefore, we consider only one case, which shows all the key features of the reflection's behavior. In discontinuous doping and periodic substrate geometries with fixed W, $\lambda_{p1} > \lambda_{p2}$ we calculate the scattering parameters versus $L < W$ by choosing eigenmodes with $n_1 > 10$. In such cases, we examine dependencies on n_2 (or $\psi = L/\lambda_{p1}$) of both the junction's scattering coefficients and those of a barrier formed by two junctions limiting the L-length region [see Figs. 3(a) and 3(c)].

It is natural to compare numerical results for scattering calculations of a barrier with the transfer-matrix approach (see the details in Appendix B). The transfer-matrix solution by a double barrier is given by the following expression:

$$\rho^{(\mathrm{TM})} = \frac{\rho_{21} + P_1^2 \rho_{12} (\tau_{12}\tau_{21} - \rho_{12}\rho_{21})}{1 - P_1^2 \rho_{12}^2}, \tag{14}$$

where $P_1 = e^{-iqL}$, q is the plasmon wavevector, L is the barrier length, i.e., a distance between the junctions, ρ_{ik}, τ_{ik} are the scattering coefficients of the individual junctions. The results for two types of junctions are presented in Figs. 6(a) and 6(b). They reveal dependence of the absolute value of the reflection coefficient from the barrier versus its normalized length L/λ_{p2}, calculated using both numerical approach and T-matrix approach, Eq. (14). The scattering coefficients ρ_{ik}, τ_{ik} substituted into Eq. (14) in the case of discontinuous-doping junctions are calculated using the exact analytical expressions Eq. (10). In the case of discontinuous substrate junctions ρ_{ik}, τ_{ik} are taken from our numerical results shown in Fig. 5(c).

The TM-based approximation predicts very accurately positions of the Fabry-Perot resonances even under the condition when it should not be applicable, i.e., at $n_2 \lesssim 0.5$. Moreover, the $\rho\,(L)$ dependence shows nonphysical behavior at $L = 0$. As it is seen from the plots, $\rho\,(L = 0) \neq 0$, but this is determined by the general relations between the complex scattering coefficients in Eq. (5). In the case of Fresnel's relations for τ and ρ, Eq. (14) gives identically zero for $\rho^{(\mathrm{TM})}$ in the limit $L = 0$. However, plasmonic scattering coefficients follow Eq. (5) and they often have nontrivial complex phases (see, for instance, Eq. (10) and Ref. [28]), which makes it impossible to turn the expression in brackets $(\tau_{12}\tau_{21} - \rho_{12}\rho_{21})$ to be identically one. Widely used phenomenological methods for calculating plasmon reflection omit its complex phase, which lead to wrong resonant peaks positions in plasmonic resonators (e.g., see comparison between the phenomenological model and the exact solution in Ref. [29]). Taking into account the general relation Eq. (5), one can conclude that preserving both correct positions of the Fabry-Perot resonances and the correct behavior of $\rho^{(\mathrm{TM})}$ at small lengths of the resonator is impossible in the framework of the pure T-matrix approach.

The numerical reflection coefficients in Figs. 6(a) and 6(b) show different behavior for even and odd Fabry-Perot resonances. The heights of the even resonances increase with the mode number, while the heights of the odd resonances decrease. A similar trend is observed in modeling plasma wave resonances excited in 2D electron channel [23]. It can be explained by the obvious difference in the total electric charge of a standing wave of the charge density inside the barrier for different types of resonances. The first resonance in Fig. 6(a) reaches 99% reflection that potentially may be exploited in designing high on:off ratio plasmonic switches. From the examples shown in Figs. 6(a) and 6(b), one can see that the full-wave calculations of the reflection coefficients relax toward the T-matrix model at $n_2 \gtrsim 5$. The number "5" comes from the dependence of the interaction length between the two junctions on both the plasmon wavelength λ_{p2} between the junctions, and λ_{p1} outside of the junction. To show this, we perform similar calculations as in Figs. 6(a) and 6(b), but for the case of "inversed" geometries (i.e., when $\lambda_{p1} < \lambda_{p2}$), see Appendix C. These calculations, and others for different junction parameters (e.g., $\lambda_{p1}/\lambda_{p2} \sim 3$, 10, 20), lead us to the conclusion that the two junctions in our periodic geometries can be modeled using the T-matrix

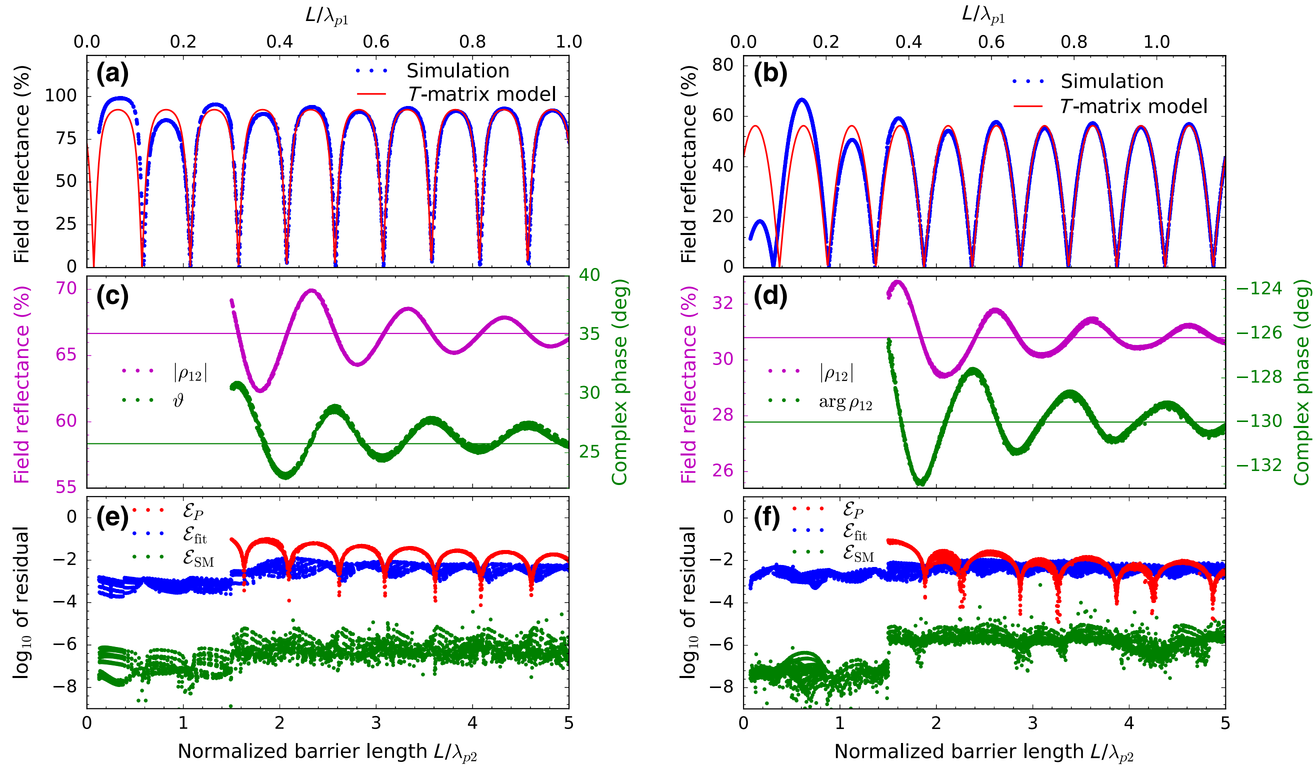

FIG. 6. Plasmon reflectance from double-junction barriers of two kinds versus barrier length normalized to the plasmon wavelength in the barrier region λ_{p2}: full-wave simulations (circles) and the T-matrix model (solid curves). (a) The barrier is formed by two discontinuous-doping junctions with two transitions between the graphene doping: $\mu_c \to 0.2\mu_c$ and $0.2\mu_c \to \mu_c$, ($\mu_c = 300$ meV, $\lambda_{p2} = 30.8$ nm), graphene is supported by homogeneous substrate with dielectric permittivity $\varepsilon_1 = 3.9$. (b) Results for the barrier formed by two discontinuous-substrate junctions: $\varepsilon_1 \to \varepsilon_2$ and $\varepsilon_2 \to \varepsilon_1$, ($\varepsilon_1 = 3.9$, $\varepsilon_2 = 20$, and $\lambda_{p2} = 35.9$ nm), Fermi energy of homogeneously doped graphene is $\mu_c = 300$ meV. (c),(d) Absolute value of ρ_{12} (purple line) and its complex phase (green line) retrieved from the same eigenmodes that are used for numerical calculating of the dependencies in the corresponding panels (a) and (b). The horizontal lines of the corresponding colors indicate the values toward to which $|\rho_{12}|$ and ϑ (or arg ρ_{12}) relax at big $n_2 = L/\lambda_{p2}$. (d),(f) Corresponding values of residuals $\mathcal{E}_P$, $\mathcal{E}_{\rm fit}$, and $\mathcal{E}_{\rm SM}$.

approach if $n_2 = \psi \gtrsim 1$ (while $W > L$ is still satisfied). For the case of barrier in Fig. 2(b), we can now formulate a trivial (but not obvious) phenomenological condition for the interaction distance between the two junctions:

$$L \gg \max\left\{\lambda_{p0}, \lambda_{p,-1}, \lambda_{p1}\right\}. \tag{15}$$

V. DISCUSSION OF THE RESULTS

To illustrate applicability of the T-matrix approach, we plot in Figs. 6(c) and 6(d) single-barrier reflection coefficients ρ_{ik} when $n_2 \geq 1.5$ and it is possible to make the fitting with the running waves. Note, that Eq. (14) gives exactly the same field reflectance from the double barrier as the numerical result, if ρ_{ik} from Figs. 6(c) and 6(d) are used instead of single-barrier solutions in Eqs. (10) and (12). The square root of $\left|\rho - \rho^{(\rm TM)}\right|^2$, averaged over all points, is less than 10^{-4}% with the maximum deviation of 0.02%.

Figures 6(e) and 6(f) show the residuals $\mathcal{E}_{\rm fit}$, $\mathcal{E}_{\rm SM}$, and $\mathcal{E}_P$ associated with the upper panels. For $n_2 < 1.5$, we do not fit numerical solutions to the running waves inside the barrier. $\mathcal{E}_P$ in that case is not shown because it is very small (about 10^{-8}). The overall fit of all the calculated modes is as perfect as in the case of a single-junction example shown in Fig. 4. The small value of $\mathcal{E}_{\rm SM}$ proves good accuracy of the numerical solutions for the charge distribution in Eq. (6). For instance, $\mathcal{E}_{\rm SM} \sim 10^{-6}$ corresponds to the relative error of ρ_{ik}, τ_{ik} of about 10^{-3}. This can be considered a very good accuracy taking into account the slow convergence of the reflection coefficient with increasing n_2, see Figs. 6(c) and 6(d).

A relatively big value of $\mathcal{E}_P \sim 10^{-2}$ can not be considered as a measure of ρ_{ik}, τ_{ik} inaccuracy. This can be explained by the example of the plasmon scattering from the gap in graphene junction. It can be viewed as a barrier formed by the two discontinuous-doping junctions in the limit of zero doping inside the barrier ($\mu_{c2} \to 0$). Since there is no current or charge density inside the gap formally we have $\tau_{12} \to 0$. This might imply that the net transmission through the double junction is also $\tau^{(\rm TM)} = 0$. However, numerical finite transmission coefficient is explained by the capacitive coupling across the gap (see, for instance, Ref. [21]) and large $\mathcal{E}_P$ demonstrates energy-flux leakage in the junction through the capacitive coupling. Moreover, this conclusion does not contradict the T-matrix model solution. Indeed, since we know that the transmission through the gap is finite, it should imply that $\tau_{21} \to \infty$. Therefore, the T-matrix expression:

$$\tau^{(\mathrm{TM})} = \frac{P_1 \tau_{12} \tau_{21}}{1 - P_1^2 \rho_{12}^2} \tag{16}$$

is undefined in this case.

As in the case of reflection, we compare transmission τ calculated through the whole barrier and τ^{TM} from the T-matrix model with the single-junction scattering coefficients ρ_{ik}, τ_{ik} obtained numerically as shown in Figs. 6(c) and 6(d). In this case, we see a perfect matching, i.e., the square root of the average of $\left|\tau - \tau^{(\mathrm{TM})}\right|^2$ is approximately 10^{-4}% and the maximal value of $\left|\tau - \tau^{(\mathrm{TM})}\right|$ is approximately 0.02%. Thus, the reflection calculations presented in Figs. 6(c) and 6(d) are not just fitting parameters in the T-matrix model. The obtained scattering coefficients ρ_{ik}, τ_{ik} both satisfy the general relationship for the S matrices in Eq. (5) and are self-consistent with the numerical solutions of the Maxwell equations. Therefore, in the case of closely packed plasmonic junctions, traditional approach for the reflection and transmission coefficients becomes invalid. As demonstrated in Figs. 6(c) and 6(d), the solutions also depend on the optical paths of the plasmon waves (n_1 and n_2 in our notations).

VI. CONCLUSIONS

In conclusion, we demonstrate that plasmon-scattering coefficients can be reconstructed directly from the numerical solutions of Maxwell equations for quasistatic plasmons with controllable accuracy. Our technique can be used to extract transmission coefficients from the numerical eigenvalue solutions for plasmons including commercial software implementing the final-element methods for potentially more complex structures. For example, the eigenmode solver of the COMSOL package is already used to calculate plasmons in some 1D plasmonic structures [30], the HFSS package has also its own eigenmode solver. We find that the limitation on the minimal length between the two junctions, when the T-matrix method is applicable, depends as well on the plasmon wavelengths outside of the junction.

VII. OUTLOOK

The spatial or temporal alternations of the dielectric environments of 1D junctions are important for innovative applications in 2D plasmonic systems. Our results facilitate designs of plasmonic resonators, topological waveguides, modulators, and photonic switches etc. based on graphene and others conducting 2D materials. Particularly, electrostatic gating, ultrafast photoexcitation, moire and substrate engineering (e.g., suspension) can be utilized to modulate the plasmon polariton propagation in on-chip 2D devices. With further advances in the lithography and sample-fabrication techniques, extreme subwavelength photon manipulation can also be expected at the visible to near-infrared telecommunication frequencies.

ACKNOWLEDGMENTS

Support was provided by the Center for Computational Research at the University at Buffalo [32]. V.P. acknowledges support from the Vice President for Research and Economic Development (VPRED) at the University at Buffalo. M.K.L. acknowledges support from the RISE2 node of NASA's Solar System Exploration Research Virtual Institute under NASA Cooperative Agreement No. 80NSSC19MO2015. This research is also partially supported by the National Science Foundation under Grant No. DMR-1904576.

APPENDIX A: GETTING PLASMON EIGENMODES

For geometries shown in Figs. 3(a) and 3(c), i.e., discontinuous-doping and substrate junctions, we apply Maxwell's equations, boundary conditions, continuity equation, and Ohm's law. These equations are reduced to a homogeneous system of linear equations, which gives both the frequency spectrum and the corresponding complex harmonics for the current density in graphene [25]. For convenience, we apply the quasistatic approximation that reduces the problem to an ordinary problem of finding eigenvalues and eigenvectors.

The complex spatial distribution of the electric field above graphene can be represented as

$$\mathbf{E}^{(0)}(x,z) = \sum_{j=-\infty}^{\infty} a_j \begin{bmatrix} i\kappa_{0,j} \\ 0 \\ q_j \end{bmatrix} e^{-iq_j x - \kappa_{0,j} z}, \tag{A1}$$

where a_j are unknown amplitudes; $q_j = K + B_0 j$ are real wavevectors, where K is a quasimomentum and $B_0 = 2\pi/d$ is the reciprocal unit cell's period. The decay rates of the evanescent waves are $\kappa_{0,j} = \sqrt{q_j^2 - \varepsilon_0(\omega^2/c^2)}$, where ε_0 is the dielectric permittivity of the medium above graphene and ω is the plasmon frequency and c is the speed of light.

For the geometry shown in Fig. 3(b), the solution cannot be easily obtained by putting graphene conductivity to zero in the corresponding areas [21]. Therefore, we start with the Poisson equation together with Ohm's law and the continuity equation [12,23]. This allows us to reduce the solution to an eigenvalues-eigenvectors problem as in the two other cases.

1. Discontinuous-doping geometry

We represent an electric field in the medium below graphene as Fourier series:

$$\mathbf{E}^{(1)}(x,z) = \sum_{j=-\infty}^{\infty} b_j \begin{bmatrix} \gamma_{1,j} \\ 0 \\ \alpha_j \end{bmatrix} e^{-iB_0(\alpha_j x - \gamma_{1,j} z)}, \qquad \text{(A2)}$$

where $\alpha_j = q_j/B_0$, $\gamma_{1,j} = \sqrt{\varepsilon_1(\omega^2/c^2) - q_j^2}/B_0$, and ε_1 is the dielectric permittivity of the medium below graphene.

Relationship between the complex current distribution $j(x)$ and the electric field component $E_x(x)$ in graphene plane is given by Ohm's law: $j(x) = \gamma_\omega(x) E_x(x)$. In a Fourier domain, the latter is reduced to

$$u_j = \sum_{l=-\infty}^{\infty} \gamma_{\omega,j-l} E_{x,l}, \qquad \text{(A3)}$$

where u_j, $E_{x,j}$, and $\gamma_{\omega,j}$ are the coefficients of the Fourier expansions of $j(x)$, $E_x(x)$, and $\gamma_\omega(x)$, correspondingly

$$j(x) = \sum_{j=-\infty}^{\infty} u_j e^{-iq_j x}, \quad E_x(x) = \sum_{j=-\infty}^{\infty} E_{x,j} e^{-iq_j x},$$
$$\gamma_\omega(x) = \sum_{j=-\infty}^{\infty} \frac{\gamma_{\omega,j}}{2} e^{-iq_j x}, \quad \gamma_{\omega,j} = \frac{2}{d}\int_{-\frac{d}{2}}^{\frac{d}{2}} \gamma_\omega(x)\, e^{ijB_0 x}. \qquad \text{(A4)}$$

We also introduce Fourier harmonics s_j of the charge density $\sigma(x)$ in graphene:

$$\sigma(x) = \sum_{j=-\infty}^{\infty} s_j e^{-iq_j x}, \qquad \text{(A5)}$$

which are connected to u_j according to $i\omega s_j = iq_j u_j$. The latter follows from the charge conservation law:

$$\frac{\partial \sigma}{\partial t} + \frac{\partial j}{\partial x} = 0. \qquad \text{(A6)}$$

We take the conductivity of a homogeneous graphene sheet according to the Drude model [see Eq. (2)] and introduce a discontinuity of the doping as

$$\mu_c(x) = \begin{cases} \mu_{c1}, & |x - nd| \le \dfrac{W}{2} \\ \mu_{c2}, & \left|x - \left(n + \dfrac{1}{2}\right)d\right| \le \dfrac{L}{2} \end{cases}, \qquad \text{(A7)}$$

Eq. (A7) allows us to reduce $\gamma_{\omega,j-l}$ to a product $\gamma_\omega \cdot \gamma_{jl}$, where γ_{jl} is a symmetric matrix, which depends only on the ratio of μ_{c2}/μ_{c1} and the geometrical scaling parameter $r = W/L$.

In summary, we have to solve the following set of equations.

(a) Boundary condition for the tangential components of the **E**-vector:

$$a_j i\kappa_{0,j} = E_{x,j}^{(1)} \qquad \text{(A8)}$$

(b) Boundary condition for the normal components of the **D**-vector:

$$\varepsilon_0 a_j q_j - D_{z,j}^{(1)} = 4\pi s_j. \qquad \text{(A9)}$$

(c) Ohm's law:

$$u_j = \gamma_\omega \sum_{l=-\infty}^{\infty} \gamma_{jl} E_{x,l}^{(1)}. \qquad \text{(A10)}$$

(d) Charge conservation equation and relationship between $D_{z,j}^{(1)}$ and $E_{x,j}^{(1)}$:

$$i\omega s_j = iq_j u_j, \quad \frac{D_{z,j}^{(1)}}{E_{x,j}^{(1)}} = \frac{\varepsilon_1 \alpha_j}{\gamma_{1,j}}. \qquad \text{(A11)}$$

These equations are reduced to the following linear system of equations:

$$\sum_{m=-\infty}^{\infty} \left[\delta_{jm} - \frac{4\pi i \gamma_\omega}{\omega} \gamma_{jm} \kappa_{0,m} R_m\right] u_m = 0, \qquad \text{(A12)}$$

where δ_{jm} is the Kronecker symbol and

$$R_j = \frac{1}{\varepsilon_0 - \varepsilon_1 \frac{i\kappa_{0,j}}{B_0 \gamma_{1,j}}}. \qquad \text{(A13)}$$

In the quasistatic approximation, when $\sqrt{\varepsilon_l}\omega/c \ll K, B_0$, $\kappa_{0,j}$, and $\gamma_{1,j}$ are equal to $|q_j|$ and $-i|\alpha_j|$, correspondingly, Eq. (A12) are reduced to an eigenvalue problem.

2. Discontinuous-substrate geometry

In this case, the electric field below graphene can be represented as a linear combination of the basis functions according to the following ansatz:

$$\mathbf{E}^{(1)}(x,z) = \begin{cases} \mathbf{E}^{(1,2)}(x,z), & -W/2 \le x < W/2 \\ \mathbf{E}^{(1,1)}(x,z), & W/2 \le x < d/2 \\ \mathbf{E}^{(1,1')}(x,z), & -d/2 \le x < -W/2 \end{cases}, \qquad \text{(A14)}$$

where

$$\mathbf{E}^{(1,2)}(x,z) = e^{i\varkappa z}\left(B^{+}\begin{bmatrix}-i\varkappa\\0\\q_{2\varkappa}\end{bmatrix}e^{-iq_{2\varkappa}\left(x+\frac{W}{2}\right)} + B^{-}\begin{bmatrix}-i\varkappa\\0\\-q_{2\varkappa}\end{bmatrix}e^{iq_{2\varkappa}\left(x-\frac{W}{2}\right)}\right), \tag{A15}$$

$$\mathbf{E}^{(1,1)}(x,z) = e^{i\varkappa z}\left(A^{+}\begin{bmatrix}-i\varkappa\\0\\q_{1\varkappa}\end{bmatrix}e^{-iq_{1\varkappa}\left(x-\frac{W}{2}\right)} + A^{-}\begin{bmatrix}-i\varkappa\\0\\-q_{1\varkappa}\end{bmatrix}e^{iq_{1\varkappa}\left(x-\left[L+\frac{W}{2}\right]\right)}\right), \tag{A16}$$

$$\mathbf{E}^{(1,1')}(x,z) = e^{i\varkappa z+i\Phi}\left(A^{+}\begin{bmatrix}-i\varkappa\\0\\q_{1\varkappa}\end{bmatrix}e^{-iq_{1\varkappa}\left(x+\left[L+\frac{W}{2}\right]\right)} + A^{-}\begin{bmatrix}-i\varkappa\\0\\-q_{1\varkappa}\end{bmatrix}e^{iq_{1\varkappa}\left(x+\frac{W}{2}\right)}\right), \tag{A17}$$

where $q_{1,2\varkappa} = \sqrt{\varkappa^2 + \varepsilon_{1,2}\omega^2/c^2}$. A similar ansatz was applied in Ref. [31] for the light diffraction on a grating problem. Matching the boundary conditions for the **E**- and **D**- vectors on the vertical bounds of the media at $x = \pm W/2$ leads to the spectral equation, from which $\varkappa = \{\varkappa_j\}, j = \overline{1..\infty}$ can be found:

$$\begin{aligned}&\cos(\varphi_1+\varphi_2)\left[2+\frac{a_2}{a_1}+\frac{a_1}{a_2}\right]\\&\quad-\cos(\varphi_1-\varphi_2)\left[\frac{a_2}{a_1}+\frac{a_1}{a_2}-2\right] = 4\cos\Phi,\\&\varphi_1 = q_{1\varkappa}L,\quad \varphi_2 = q_{2\varkappa}W,\quad a_1 = \frac{\varepsilon_1}{q_{1\varkappa}},\quad a_2 = \frac{\varepsilon_2}{q_{2\varkappa}}.\end{aligned} \tag{A18}$$

For convenience, we consider a dielectric media with permittivity independent of ω and zero imaginary part, i.e., $\operatorname{Im}\varepsilon_m = 0$. The quasistatic approximation gives $q_{1\varkappa} = q_{2\varkappa} = \varkappa$. Once the $\varkappa$ spectrum is found, it is possible to retrieve amplitudes A^+, A^-, B^+, and B^-. Any $\mathbf{E}^{(1)}(x,z)$ function is a linear combination of the basis functions $\mathbf{E}^{(1)}_{\varkappa}(x,z)$:

$$\mathbf{E}^{(1)}(x,z) = \sum_{\varkappa} C_{\varkappa}\mathbf{E}^{(1)}_{\varkappa}(x,z). \tag{A19}$$

To find $C_{\varkappa}$, we need to match the tangential component of the electric field below graphene $E_\tau(x) = \sum_{\varkappa} C_{\varkappa}E_{\tau,\varkappa}$ and the normal component of the electrical displacement vector $D_n(x) = \sum_{\varkappa} C_{\varkappa}D_{n,\varkappa}$, where

$$E_{\tau,\varkappa} = E^{(1)}_{x,\varkappa}\Big|_{z=0},\quad D_{n,\varkappa} = \varepsilon_1(x)\,E^{(1)}_{z,\varkappa}\Big|_{z=0}, \tag{A20}$$

$$\varepsilon_1(x) = \begin{cases}\varepsilon_2, & -\dfrac{W}{2} \le x - nd < \dfrac{W}{2}\\ \varepsilon_1, & -\dfrac{L}{2} \le x - \left(n+\dfrac{1}{2}\right)d < \frac{L}{2}\end{cases},\quad n\in\mathbb{Z}. \tag{A21}$$

Then we expand the basis functions into the Fourier series:

$$E_{\tau,\varkappa}(x) = \sum_{j=-\infty}^{\infty}\varepsilon_{\varkappa j}e^{-iq_jx},\quad D_{n,\varkappa}(x) = \sum_{j=-\infty}^{\infty}\Delta_{\varkappa j}e^{-iq_jx}. \tag{A22}$$

The equations for $C_{\varkappa}$ follow from a set of equations.

(a) Boundary condition for the tangential components of the **E**-vector:

$$a_j\,i\kappa_{0,j} = \sum_{\varkappa} C_{\varkappa}\varepsilon_{\varkappa j}. \tag{A23}$$

(b) Boundary condition for the normal components of the **D**-vector:

$$\varepsilon_0 a_j q_j - \sum_{\varkappa} C_{\varkappa}\Delta_{\varkappa j} = 4\pi s_j. \tag{A24}$$

(c) Ohm's law and charge conservation equation:

$$u_j = \gamma_\omega\sum_{\varkappa} C_{\varkappa}\varepsilon_{\varkappa j}\quad i\omega s_j = iq_j u_j. \tag{A25}$$

The boundary conditions are reduced to a homogeneous system of linear equations:

$$\sum_{l=1}^{2N+1}\left(A_{jl} - \Lambda\delta_{jl}\right)C_{\varkappa_l} = 0, \tag{A26}$$

where $\Lambda = \omega/(i\gamma_\omega 4\pi B_0)$, $N \sim 1000$ is the Fourier expansion truncation number, and A_{jl} form a square matrix that can be calculated as

$$A = \left\{ \varepsilon_0 \frac{q_j}{\kappa_{0,j}} \varepsilon_{\varkappa j} - i\Delta_{\varkappa j} \right\}^{-1} \cdot \left\{ \alpha_j \varepsilon_{\varkappa j} \right\}, \quad \text{(A27)}$$

where the curly braces must be considered as operators converting the function of two variables $f\,(j,\varkappa)$ to the matrix M as follows:

$$\begin{aligned} M &= \{f\ (j,\varkappa)\}, \quad M_{jl} = f\ (j,\varkappa_l), \\ j &= \overline{-N\,..\,N}, \quad l = \overline{1\,..\,2N+1}. \end{aligned} \quad \text{(A28)}$$

The obtained matrix Eq. (A26) together with the spectral Eq. (A18) work also without the quasistatic approximation. But in that case, solution of Eq. (A28) involves additional computational efforts, which are beyond the scope of this work.

3. Gap in graphene geometry

The solution for a similar problem, but for the case of zero-quasi-momentum (K, $\Phi = 0$) was presented in Ref. [25]. The method of describing plasma waves in 2D electron systems within the quasistatic approximation involving an integral equation was presented in Refs. [12,23]. In the case of the quasistatic approximation, there are only three unknown functions: a sheet charge density $\sigma\,(x,t)$, a linear current per graphene stripe length $I\,(x,t)$, and an electric field's tangential component $E^i_x\,(x,t)$ in graphene. As before, we represent these functions in terms of the complex amplitudes $\sigma_\omega\,(x)$, $I_\omega\,(x)$, and $E^i_{x\omega}\,(x)$:

$$\begin{aligned} \sigma\,(x,t) &= \mathrm{Re}\left[e^{i\omega t}\sigma_\omega\,(x)\right], \\ I\,(x,t) &= \mathrm{Re}\left[e^{i\omega t}I_\omega\,(x)\right], \\ E^i_x\,(x,t) &= \mathrm{Re}\left[e^{i\omega t}E^i_{x\omega}\,(x)\right]. \end{aligned} \quad \text{(A29)}$$

These distributions are connected with each other by the following equations.

(a) Charge conservation:

$$i\omega\sigma_\omega\,(x) + \frac{\partial}{\partial x} I_\omega\,(x) = 0. \quad \text{(A30)}$$

(b) Ohm's law:

$$I_\omega\,(x) = \gamma_\omega E^i_{x\omega}\,(x), \quad \text{(A31)}$$

(c) Poisson equation:

$$E^i_{x\omega}\,(x) = \frac{1}{\varkappa}\int_{-\infty}^{\infty} \frac{2\sigma_\omega(x')\,dx'}{x-x'}, \quad \varkappa = \frac{\varepsilon_0+\varepsilon_1}{2}, \quad \text{(A32)}$$

(d) Boundary conditions for the current at the graphene stripe edges: $I_\omega\,(\pm W/2) = 0$.

According to Bloch's theorem, oscillations at any two adjacent graphene stripes differ only by a phase factor: $\sigma_\omega\,(x+d) = \sigma_\omega\,(x)\,e^{-i\Phi}$, where d is the system's period. Using the symmetry property of $\sigma_\omega\,(x)$, Eq. (A32) can be reduced to an integral:

$$\begin{aligned} \varkappa E^i_{x\omega}\,(x) &= \int_{-W/2}^{W/2} \frac{2\sigma_\omega(x')\,dx'}{x-x'} + \sum_{k=1}^{\infty} \\ &\times \int_{-W/2}^{W/2} \left[\frac{2e^{-ik\Phi}}{x-x'-kd} + \frac{2e^{ik\Phi}}{x-x'+kd}\right] \\ &\times \sigma_\omega(x')\,dx'. \end{aligned} \quad \text{(A33)}$$

The Fourier series are defined as follows:

$$\begin{aligned} F\,(x) &= \frac{1}{2}\sum_{j=-\infty}^{\infty} f_j\,e^{-iB_W jx}, \\ f_j &= \frac{2}{W}\int_{-W/2}^{W/2} F\,(x)\,e^{iB_W jx}\,dx, \end{aligned} \quad \text{(A34)}$$

where $F\,(x)$ stands for the spatial distributions of $\sigma_\omega\,(x)$, $I_\omega\,(x)$, or $E^i_{x\omega}\,(x)$, and $B_W = 2\pi/W$. We obtain the following system of linear equations for u_l and the frequency ω of the plasmon modes:

$$\begin{cases} \sum_{l=-N}^{N}\left(M_{jl} - \Lambda\delta_{jl}\right)u_l = 0, & \Lambda = \dfrac{\omega}{i\gamma_\omega}\dfrac{\varkappa}{\pi B_W} \\ \sum_{l=-N}^{N}(-1)^l\,u_l = 0, \end{cases} \quad \text{(A35)}$$

where N is a number of the Fourier harmonics, δ_{jl} is Kronecker's symbol, and

$$\begin{aligned} M_{jl} &= M^{(0)}_{jl} + \sum_{k=1}^{K_{\mathrm{nb}}}\left[M^{(k,\mathrm{a})}_{jl}\cos k\Phi - M^{(k,\mathrm{s})}_{jl}\sin k\Phi\right], \\ M^{(0)}_{jl} &= \frac{l}{\pi i}\frac{2}{W}\int_{-W/2}^{W/2}\int_{-W/2}^{W/2}\frac{e^{iB_W(jx-lx')}}{x-x'}dxdx', \\ M^{(k,\mathrm{a})}_{jl} &= \frac{2l}{\pi i}\frac{2}{W}\int_{-W/2}^{W/2}\int_{-W/2}^{W/2}\frac{\left(x-x'\right)e^{iB_W(jx-lx')}}{(x-x')^2-k^2d^2}dxdx', \\ M^{(k,\mathrm{s})}_{jl} &= \frac{2l}{\pi}\frac{2}{W}\int_{-W/2}^{W/2}\int_{-W/2}^{W/2}\frac{kde^{iB_W(jx-lx')}}{(x-x')^2-k^2d^2}dxdx', \end{aligned} \quad \text{(A36)}$$

where K_{nb} is the maximum number of the neighboring unit cells. The double-integrals in M_{jl} can be reduced to a single-dimensional integral over new variable $x-x'$. In our calculations, we use $N = 1000$ and $K_{\mathrm{nb}} = 1$.

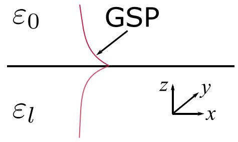

FIG. 7. Schematics of a plasmon in graphene separating two media.

APPENDIX B: RETRIEVING THE SCATTERING MATRIX

For each set of the plasmonic structure parameters, we calculate lengths W (and L if applicable) which are expected to give good plasmonic modes for calculating the scattering parameters. We fix a basis plasmon energy (in our calculations it is always put to 100 meV) and calculate the plasmon wavelengths λ_{p1}, λ_{p2} in each region supporting plasmons. Then the lengths are calculated using this heuristic formulas:

$$W, L = 10 \max\left\{\lambda_{p1}, \lambda_{p2}\right\}. \tag{B1}$$

The numerical solutions for plasmon eigenmodes are obtained by our solvers in the following form:

$$\sigma_l(x,t) = \mathrm{Re}\left\{e^{i\omega t}\sigma_\omega^{(l)}(x)\right\}, \quad \sigma_\omega^{(l)}(x) = \sum_{j=-N}^{N} s_{l,j}\, e^{-iB_0 jx}, \tag{B2}$$

where $l \in \overline{1\,..\,2N+1}$ is the eigenmode's index, $B_0 = 2\pi/d$ is the reciprocal lattice's period.

For a given l, its own eigenfrequency determines the plasmon wavelengths λ_{p1} and λ_{p2} in the corresponding areas in Figs. 3(a)–3(c). We choose the solutions that have as least several plasmon wavelengths on both sides of the junction:

$$W, L \gtrsim 10 \max\left\{\lambda_{p1}, \lambda_{p2}\right\}.$$

At the same time, the Fourier resolution should be fine, i.e., $\min\{\lambda_{p1}, \lambda_{p2}\} \gtrsim 7 \cdot d/N$, where $d = W + L$ is the unit cell length.

For each numerical solution for the charge density distribution $\sigma_\omega(x)$, the amplitudes $A_1^{(0)}, B_1^{(0)}$ and $A_2^{(0)}, B_2^{(0)}$ can be found from the fit to the following function:

$$\sigma_\omega^{(\mathrm{model})} = A \exp\left[-iq\left(x - x_L\right)\right] + B \exp\left[iq\left(x - x_R\right)\right],$$
$$x \in \left[x_L + \frac{\lambda_p}{2}\,..\,x_R - \frac{\lambda_p}{2}\right], \tag{B3}$$

where the fitting parameters A and B are complex and the wavevector q is real. The left and right bounds of the junction are x_L and x_R, correspondingly. An example of the calculated $\sigma_\omega(x)$, with the corresponding fits, is shown in Fig. 4.

Once all the amplitudes of the running waves are retrieved, the scattering matrix [for cases in Figs. 3(a) and (c)] can be found from the following equation:

$$S_{12}\begin{bmatrix} A_1^{(0)}P_1 & B_1^{(0)}P_1P \\ B_2^{(0)}P_2 & A_2^{(0)}P_2 \end{bmatrix} = \begin{bmatrix} A_2^{(0)} & B_2^{(0)} \\ B_1^{(0)} & A_1^{(0)}P \end{bmatrix}, \tag{B4}$$

where $P_1 = e^{-iq_1W}$, $P_2 = e^{-iq_2L}$, and $P = e^{-i\Phi}$ are the phase factors gained by the waves, and Φ is the phase shift between the adjacent unit cells.

Equation (B4) can be reduced to the case of the gap in graphene junction [see Fig. 3(b)] with the following substitutions: $P_2 \to P_1$, $P \to 2P$, $A_2^{(0)} \to A_1^{(0)}P$, and $B_2^{(0)} \to B_1^{(0)}P$. The symmetric scattering matrix S_{11} is given by

$$S_{11}\begin{bmatrix} A_1^{(0)}P_1 & B_1^{(0)}P_1P \\ B_1^{(0)}P_1P & A_1^{(0)}P_1 \end{bmatrix} = \begin{bmatrix} A_1^{(0)}P & B_1^{(0)} \\ B_1^{(0)} & A_1^{(0)}P \end{bmatrix}. \tag{B5}$$

1. Energy carried by the plasmon

Let us consider a plasmon in graphene as shown in Fig. 7. The sheet charge density wave in graphene is given by $\sigma(x,t) = \mathrm{Re}\,\sigma_\omega e^{i\omega t - iqx}$, where σ_ω is the plasmon's complex amplitude, ω is its frequency and q is the wavevector. Having calculated **E** and **H** fields, one can obtain the time-averaged energy flux per unit length in y direction carried by the plasmon $\mathbf{S} = (c/4\pi)\int_{-\infty}^{\infty}\langle\mathbf{E}\times\mathbf{H}\rangle\, dz$, which absolute value scales with the square of the charge density amplitude $|\mathbf{S}| = s_l\,|\sigma_\omega|^2$, where

$$s_l = \frac{\omega^3 \mathbf{Re}\, q}{16\pi\,|\gamma_\omega q|^2}\left(\frac{\varepsilon_0}{|\varkappa_0|^2\,\mathbf{Re}\varkappa_0} + \frac{\varepsilon_l}{|\varkappa_l|^2\,\mathbf{Re}\varkappa_l}\right), \tag{B6}$$

where $\varkappa_{0,l} = \sqrt{q^2 - \varepsilon_{0,l}\omega^2/c^2}$, $\mathrm{Re}\,\varkappa_{0,l} > 0$, are the rates of the evanescent electromagnetic fields along the z direction above and below graphene, correspondingly. In

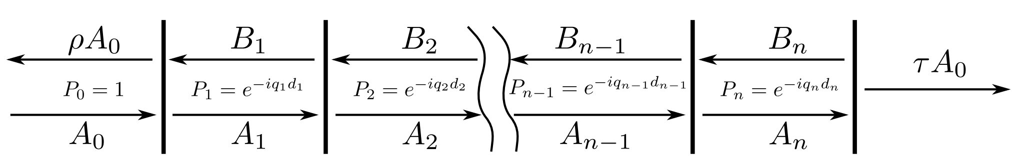

FIG. 8. Schematics of a plasmon scattering by multiple junctions.

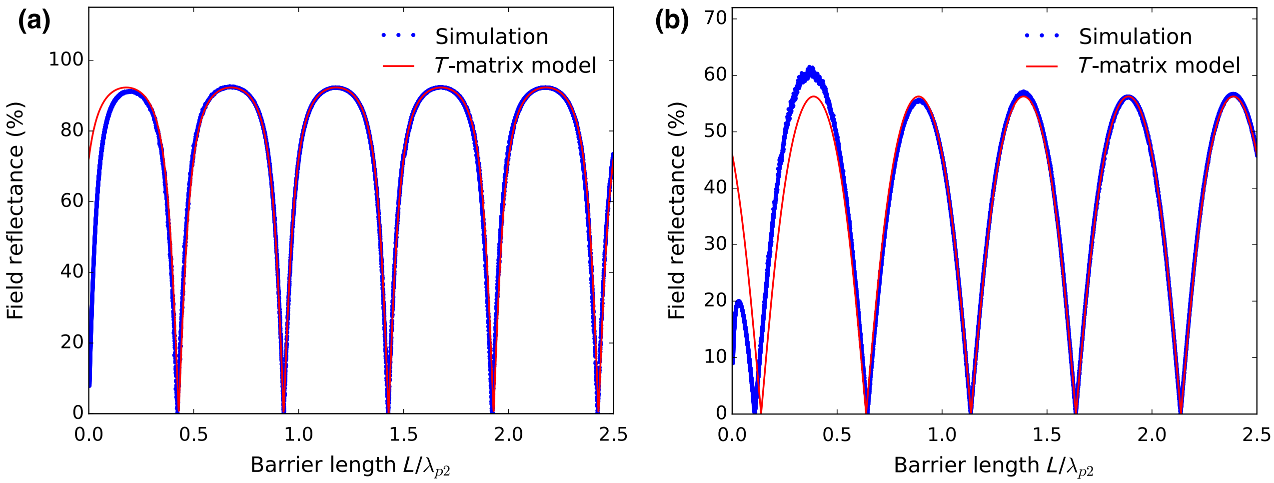

FIG. 9. Plasmon reflectance in the cases of double-junction barriers of two kinds versus barrier length normalized to the plasmon wavelength in the barrier region λ_{p2}: full-wave simulations (circles) and the T-matrix model (solid curves). (a) Results for the barrier formed by the two discontinuous-doping junctions: $\mu_{c1} \to \mu_{c2}$ and $\mu_{c2} \to \mu_{c1}$, ($\mu_{c1} = 60$ meV, $\mu_{c2} = 300$ meV, $\lambda_{p2} = 153.9$ nm) in graphene on the substrate with $\varepsilon_1 = 3.9$. (b) Results for the barrier formed by the two discontinuous-substrate junctions: $\varepsilon_1 \to \varepsilon_2$ and $\varepsilon_2 \to \varepsilon_1$, ($\varepsilon_1 = 20$, $\varepsilon_2 = 3.9$, $\lambda_{p2} = 153.9$ nm) and the doping level of graphene is 300 meV. The calculations use $N = 2000$.

the quasistatic approximation, Eq. (B6) reduces to $s_l \propto |\gamma_\omega|^2 / (\varepsilon_0 + \varepsilon_l)^3$.

Therefore, once the s_1 and s_2 coefficients and the scattering coefficients ρ_{12} and τ_{12} are known, the corresponding energy reflection and transmission coefficients can be calculated as

$$R_{12} = |\rho_{12}|^2 \quad T_{12} = |\tau_{12}|^2 \frac{s_2}{s_1}. \tag{B7}$$

2. Transfer matrices for plasmon scattering on multiple junctions

It is easy to obtain the reflection and transmission for a generalized case of n subsequent regions $j = \overline{1..n}$ of lengths d_j with the plasmon wave vectors q_j. The incident plasmon is labeled by $j = 0$ and transmitted plasmon by $j = n + 1$. Provided that the scattering coefficients ρ_{ik}, τ_{ik} of each junction at the interfaces between j and $j + 1$ are known, the resulting scattering coefficients (see Fig. 8) follow from

$$\begin{aligned} &\tau = \frac{1}{\xi_0}, \quad \rho = \frac{\xi_1}{\xi_0}, \quad \xi = \left(\prod_{i=0}^{n-1} T_i\right)\zeta, \quad \zeta = \frac{1}{P_n \tau_{n,n+1}} \begin{bmatrix} 1 \\ P_n \rho_{n,n+1} \end{bmatrix}, \\ &T_i = \frac{1}{P_j \tau_{j,j+1}} \begin{bmatrix} 1 & -P_{j+1}\rho_{j+1,j} \\ P_j \rho_{j,j+1} & P_j P_{j+1}\left(\tau_{j,j+1}\tau_{j+1,j} - \rho_{j,j+1}\rho_{j+1,j}\right) \end{bmatrix}, \end{aligned} \tag{B8}$$

where $P_0 = 1$ and $P_j = e^{-iq_j d_j}$ for $j = \overline{1..n}$, d_j is length of the region between the junctions with indices j and $j + 1$.

APPENDIX C: ADDITIONAL DATA ON THE REFLECTION BY A DOUBLE BARRIER

Figure 9 shows that full-wave reflection relaxes toward the T-matrix model in about $0.5\lambda_{p2}$ in the cases, when the plasmon wavelength inside the barrier is significantly longer than outside of it.

A notably larger numerical noise around the first resonance in Fig. 9(b) is caused by the difficulties in preserving a big enough value of n_1 for the capacitive coupling between the junctions, at length W apart, to be negligible. Filtering appropriate values of $n_1 > 10 \cdot \lambda_{p2}/\lambda_{p1}$ reduces the numerical noise and removes the data points in the interval of L/λ_{p2} of about [0.01, 0.1] in Fig. 9(a) and about [0.2, 0.5] in Fig. 9(b). The origin of this noise is not a lack of the numerical accuracy, but the dependence of the scattering coefficients on the optical paths of the scattered waves because of the capacitive coupling between the junctions. The only way to get rid of it is to satisfy the following condition: $W, L \gg \max\{\lambda_{p1}, \lambda_{p2}\}$.

[1] L. Ju, B. Geng, J. Horng, C. Girit, M. Martin, Z. Hao, H. A. Bechtel, X. Liang, A. Zettl, Y. R. Shen, and F. Wang, Graphene plasmonics for tunable terahertz metamaterials, Nat. Nanotechnol. **6**, 630 (2011).

[2] A. Vakil and N. Engheta, Transformation optics using graphene, Science **332**, 1291 (2011).

[3] A. N. Grigorenko, M. Polini, and K. S. Novoselov, Graphene plasmonics, Nat. Photonics **6**, 749 (2012).

[4] H. Yan, X. Li, B. Chandra, G. Tulevski, Y. Wu, M. Freitag, W. Zhu, P. Avouris, and F. Xia, Tunable infrared plasmonic devices using graphene/insulator stacks, Nat. Nanotechnol. **7**, 330 (2012).

[5] Z. Fei, A. S. Rodin, G. O. Andreev, W. Bao, A. S. McLeod, M. Wagner, L. M. Zhang, Z. Zhao, M. Thiemens, G. Dominguez, M. M. Fogler, A. H. C. Neto, C. N. Lau, F. Keilmann, and D. N. Basov, Gate-tuning of graphene plasmons revealed by infrared nano-imaging, Nature **487**, 82 (2012).

[6] T. Low and P. Avouris, Graphene plasmonics for terahertz to mid-infrared applications, ACS Photonics **8**, 1086 (2014).

[7] P.-Y. Chen, H. Huang, D. Akinwande, and A. Alù, Graphene-based plasmonic platform for reconfigurable terahertz nanodevices, ACS Photonics **1**, 647 (2014).

[8] A. Woessner, Y. Gao, I. Torre, M. Lundeberg, C. Tan, K. Watanabe, T. Taniguchi, R. Hillenbrand, J. Hone, M. Polini, and F. Koppens, Electrical 2π phase control of infrared light in a 350-nm footprint using graphene plasmons, Nat. Photonics **11**, 421 (2017).

[9] L. Xiong, F. C. M. Jung, A. McLeod, S. Sunku, Y. Shao, G. Ni, A. Sternbach, S. Liu, J. Edgar, E. Mele, M. Fogler, G. Shvets, C. Dean, and D. N. Basov, Photonic crystal for graphene plasmons, Nat. Commun. **10**, 4780 (2019).

[10] A. Fali, S. T. White, T. G. Folland, M. He, N. A. Aghamiri, S. Liu, J. H. Edgar, J. D. Caldwell, R. F. Haglund, and Y. Abate, Refractive index-based control of hyperbolic phonon-polariton propagation, Nano Lett. **19**, 7725 (2019).

[11] J. L. Garcia-Pomar, A. Y. Nikitin, and L. Martin-Moreno, Scattering of graphene plasmons by defects in the graphene sheet, ACS Nano **7**, 4988 (2013).

[12] B. Rejaei and A. Khavasi, Scattering of surface plasmons on graphene by a discontinuity in surface conductivity, J. Opt. **17**, 075002 (2015).

[13] S. Farajollahi, B. Rejaei, and A. Khavasi, Reflection and transmission of obliquely incident graphene plasmons by discontinuities in surface conductivity: Observation of the brewster-like effect, J. Opt. **18**, 075005 (2016).

[14] S. Farajollahi, S. AbdollahRamezani, K. Arik, B. Rejae, and A. Khavasi, Circuit model for plasmons on graphene with one dimensional conductivity profile, IEEE Photon. Technol. Lett. **28**, 355 (2016).

[15] Y. V. Bludov, N. M. R. Peres, G. Smirnov, and M. I. Vasilevskiy, Scattering of surface plasmon polaritons in a graphene multilayer photonic crystal with inhomogeneous doping, Phys. Rev. B **93**, 245425 (2016).

[16] A. J. Chaves, B. Amorim, Y. V. Bludov, P. A. D. Goncalves, and N. M. R. Peres, Scattering of graphene plasmons at abrupt interfaces: An analytic and numeric study, Phys. Rev. B **97**, 035434 (2018).

[17] X. Lin, Y. Yang, N. Rivera, J. J. López, Y. Shen, I. Kaminer, H. Chen, B. Zhang, J. D. Joannopoulos, and M. Soljačić, All-angle negative refraction of highly squeezed plasmon and phonon polaritons in graphene—boron nitride heterostructures, PNAS **114**, 6717 (2017).

[18] Z. Fei, A. S. Rodin, W. Gannett, S. Dai, W. Regan, M. Wagner, M. K. Liu, A. S. McLeod, G. Dominguez, M. Thiemens, A. H. Castro Neto, F. Keilmann, A. Zettl, R. Hillenbrand, M. M. Fogler, and D. N. Basov, Electronic and plasmonic phenomena at graphene grain boundaries, Nat. Nanotechnol. **8**, 821 (2013).

[19] L. Jiang, Z. Shi, B. Zeng, S. Wang, J.-H. Kang, T. Joshi, C. Jin, L. Ju, J. Kim, T. Lyu, Y.-R. Shen, M. Crommie, H.-J. Gao, and F. Wang, Soliton-dependent plasmon reflection at bilayer graphene domain walls, Nat. Mat. **15**, 840 (2016).

[20] Z. Fei, G.-X. Ni, B.-Y. Jiang, M. M. Fogler, and D. N. Basov, Nanoplasmonic phenomena at electronic boundaries in graphene, ACS Photonics **4**, 2971 (2017).

[21] B.-Y. Jiang, E. J. Mele, and M. Fogler, Theory of plasmon reflection by a 1d junction, Opt. Express **26**, 17209 (2018).

[22] T. M. Slipchenko, M. L. Nesterov, R. Hillenbrand, A. Y. Nikitin, and L. Martin-Moreno, Graphene plasmon reflection by corrugations, ACS Photonics **4**, 3081 (2017).

[23] A. V. Arsenin, A. D. Gladun, V. G. Leiman, V. L. Semenenko, and V. I. Ryzhii, Plasma oscillations of the two-dimensional electron gas in the field-effect transistor with a cylindrical gate electrode, J. Commun. Technol. Electron. **55**, 1285 (2010).

[24] S. Siaber, S. Zonetti, and O. Sydoruk, Junctions between two-dimensional plasmonic waveguides in the presence of retardation, J. Opt. **21**, 105002 (2019).

[25] V. Semenenko, S. Schuler, A. Centeno, A. Zurutuza, T. Mueller, and V. Perebeinos, Plasmon-plasmon interactions and radiative damping of graphene plasmons, ACS Photonics **5**, 3459 (2018).

[26] G. W. Hanson, Dyadic Green's functions and guided surface waves for a surface conductivity model of graphene, J. Appl. Phys. **103**, 064302 (2008).

[27] R. E. Collin, *Foundations for Microwave Engineering*, The IEEE Press Series on Electromagnetic Wave Theory (IEEE Press, New York NY, 2001), 2nd ed.

[28] A. Y. Nikitin, T. Low, and L. Martin-Moreno, Anomalous reflection phase of graphene plasmons and its influence on resonators, Phys. Rev. B **90**, 041407 (2014).

[29] D. Svintsov, Exact Solution for Driven Oscillations in Plasmonic Field-Effect Transistors, Phys. Rev. Appl. **10**, 024037 (2018).

[30] O. Sydoruk, K. Choonee, and G. Dyer, Transmission and reflection of terahertz plasmons in two-dimensional plasmonic devices, IEEE Trans. Terahertz. Sci. Technol. **5**, 486 (2015).

[31] P. Sheng, R. S. Stepleman, and P. N. Sanda, Exact eigenfunctions of square-wave gratings: Application to diffraction and surfacce-plasmon calculation, Phys. Rev. B **26**, 2907 (1982).

[32] Center for Computational Research, University at Buffalo, http://hdl.handle.net/10477/79221.